



Bragg gratings in bulk media
by Andrew John Heltborg

A thesis submitted in partial fulfillment of the requirements for the degree of Master of Science in
Electrical Engineering
Montana State University
© Copyright by Andrew John Heltborg (2000)

Abstract:

This thesis investigates the creation of distributed Bragg reflectors in bulk optical materials for lasers and sensors. The underlying hypothesis of this thesis is the supposition that crystal growth techniques can result in the formation of precisely defined periodic variations in the refractive index of a crystalline or glassy solid. Crystals of CTH:YAG and Tm:YAG were fabricated utilizing various growth techniques. The crystals were characterized using SEM cathodoluminescence (CL) imaging and spectra, optical diffraction techniques, and mid-infrared transmission and reflection measurements. The CTH:YAG crystals showed a periodic variation in dopant concentrations (striae) using the CL imaging. The CL spectra were used to determine that most of the striae were due to thulium (Tm^{3+}) with some contribution from chromium (Cr^{3+}) and minimal contribution from holmium (Ho^{3+}). The Tm:YAG crystals showed no striae with any of the measurement techniques. Optical diffraction was used to measure the pitch of the Bragg gratings to verify the SEM CL data. The search for Bragg reflections from the crystals is still ongoing. This data proves that the growth techniques are viable methods to produce Bragg gratings in bulk optical material.

BRAGG GRATINGS IN BULK MEDIA

by

Andrew John Heltborg

A thesis submitted in partial fulfillment
of the requirements for the degree

of

Master of Science

in

Electrical Engineering

MONTANA STATE UNIVERSITY
Bozeman, Montana

May 2000

N378
H3698

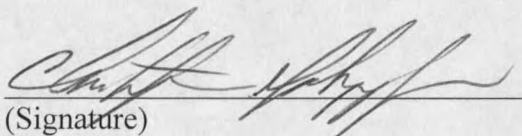
APPROVAL

of a thesis submitted by

Andrew John Heltborg

This thesis has been read by each member of the thesis committee and has been found to be satisfactory regarding content, English usage, format, citations, bibliographic style, and consistency, and is ready for submission to the College of Graduate Studies.

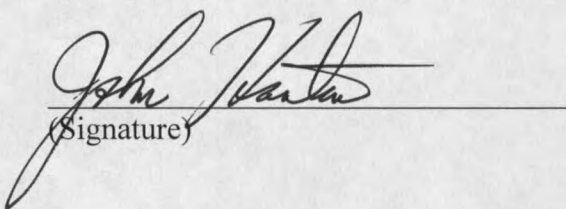
Chris Yakymyshyn
Committee Chair


(Signature)

April 11, 2000
(Date)

Approved for the Department of Electrical & Computer Engineering

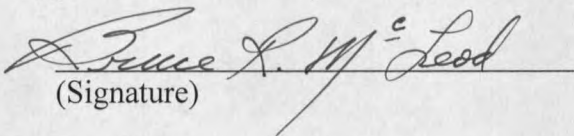
John Hanton
Department Head


(Signature)

4-11-00
(Date)

Approved for the College of Graduate Studies

Bruce McLeod
Graduate Dean


(Signature)

4-13-00
(Date)

STATEMENT OF PERMISSION TO USE

In presenting this thesis in partial fulfillment of the requirements for a master's degree at Montana State University, I agree that the Library shall make it available to borrowers under the rules of the Library.

If I have indicated my intention to copyright this thesis by including a copyright notice page, copying is allowable only for scholarly purposes, consistent with "fair use" as prescribed in the U.S. Copyright Law. Requests for permission for extended quotation from or reproduction of this thesis in whole or in parts may be granted only by the copyright holder.

Signature



Date

April 11, 2000

TABLE OF CONTENTS

1. INTRODUCTION.....	1
2. THEORY.....	5
Coupled Mode Theory.....	5
Modeling.....	11
Mathcad.....	11
Specview.....	14
Temperature and Pressure Model.....	15
3. CZOCHRALSKI GROWTH METHOD.....	18
Periodic Striae.....	20
Off Thermal Center.....	20
Varied Pull Rates.....	21
4. EXPERIMENTAL SETUPS AND RESULTS.....	22
Scanning Electron Microscope.....	22
Cathodoluminescence.....	22
X-ray Analysis.....	28
Optical Characterization.....	29
Optical Spectrum Analyzer.....	31
Optical Diffraction.....	32
Bragg Reflection Measurements.....	40
Real Time Scanning Monochromator.....	41
Single Sweep Monochromator.....	43
5. CONCLUSIONS.....	49
BIBLIOGRAPHY.....	51
APPENDICES.....	52
APPENDIX A.....	53
Mathcad Reflectance Program.....	54
APPENDIX B.....	55
Crystal List.....	56
APPENDIX C.....	57
Monochromator Filter Test.....	58

LIST OF TABLES

Table		Page
2-1.	Material Properties of YAG.....	15
B-1.	List of Crystals.....	56

LIST OF FIGURES

Figure	Page
2-1. Mode powers of the incident mode ($A(x)$) and the reflected mode ($B(x)$) in a periodic layered medium when $\Delta\beta=0$	9
2-2. Reflectance from a 5mm and 10mm crystal.....	12
2-3. Reflectance from a 10mm crystal with a modulation depth of $1 \cdot 10^{-5}$	13
2-4. Reflectance from a crystal with a 10° angle of incidence.....	14
2-5. Reflectance from a Bragg grating in YAG at different temperatures.....	16
2-6. Reflectance from a Bragg grating in YAG due to pressure changes.....	17
3-1. Schematic of a Czochralski furnace.....	19
4-1. SEM CL image of sample 1-525B showing structured, broadband CL emission.....	23
4-2. CL emission spectrum for sample 1-525B, CTH:YAG.....	24
4-3. SEM CL image from CTH:YAG sample 1-525B at a detection wavelength of 362.7nm.....	25
4-4. SEM CL image from CTH:YAG sample 1-525B at a detection wavelength of 470.4nm.....	26
4-5. SEM CL image from CTH:YAG sample 1-525B at a detection wavelength of 716.6nm.....	26

LIST OF FIGURES – CONTINUED

Figure		Page
4-6.	Optical spectrum analyzer backreflection setup.....	31
4-7.	Small angle diffraction experimental setup.....	32
4-8.	Diffraction pattern at 543.5nm from sample 1-525B.....	33
4-9.	Transmission window of YAG.....	41
4-10.	Layout of first reflectance station.....	42
4-11.	Reflectance layout using the monochromator.....	44
4-12.	Revised Monochromator setup.....	45
4-13	Transmission of 4 μ m to 6 μ m light through crystal 2-561....	47
4-14	Normalized transmission of 4 μ m to 6 μ m light light through crystal 2-561.....	48
C-1	Monochromator measurement of 2300nm bandpass filter...	58
C-2	Monochromator measurement of 4550nm bandpass filter...	58
C-3	Monochromator measurement of 5750nm bandpass filter...	59

ABSTRACT

This thesis investigates the creation of distributed Bragg reflectors in bulk optical materials for lasers and sensors. The underlying hypothesis of this thesis is the supposition that crystal growth techniques can result in the formation of precisely defined periodic variations in the refractive index of a crystalline or glassy solid. Crystals of CTH:YAG and Tm:YAG were fabricated utilizing various growth techniques. The crystals were characterized using SEM cathodoluminescence (CL) imaging and spectra, optical diffraction techniques, and mid-infrared transmission and reflection measurements. The CTH:YAG crystals showed a periodic variation in dopant concentrations (striae) using the CL imaging. The CL spectra were used to determine that most of the striae were due to thulium (Tm^{3+}) with some contribution from chromium (Cr^{3+}) and minimal contribution from holmium (Ho^{3+}). The Tm:YAG crystals showed no striae with any of the measurement techniques. Optical diffraction was used to measure the pitch of the Bragg gratings to verify the SEM CL data. The search for Bragg reflections from the crystals is still ongoing. This data proves that the growth techniques are viable methods to produce Bragg gratings in bulk optical material.

CHAPTER 1

INTRODUCTION

Electromagnetic wave propagation in periodic layered media exhibits some interesting and useful phenomena. The simplest example of a periodic layered structure consists of alternating layers of two different materials of equal thickness. This layered structure can also be made in a single material that has periodic variations in the complex refractive index. Light experiences Fresnel reflections from dielectric interfaces due to variations in the index of refraction. The light reflected from each individual interface is quite small, but if the phase delay of the reflected light is chosen correctly, each reflection adds constructively. It is possible to achieve extremely high reflectance by increasing the number of interfaces. When this phenomenon occurs with light it is referred to as either a distributed Bragg reflector (DBR) or a distributive feedback (DFB) structure.

Over the past 15 years, there has been great success in placing DFB and DBR structures in optical fibers (Culshaw) and semiconductor lasers (Luo). Fiber Bragg gratings are now commercially available and are used in various applications, including optical filtering for optical telecommunications, laser diode spectral control, and fiber sensors. DFB semiconductor lasers are very stable sources with extremely narrow linewidths that make them ideal for long-haul fiber optic telecommunications.

These structures are now being placed in bulk media. Different methods of creating these structures have been tested for dye laser doped polymeric films (Kogelnik) and with color center lasers in alkali halide crystals (Bjorkland). There have not been any investigations into using the more common and useful inorganic oxide/fluoride laser crystals and glasses. Successfully creating a DFB or DBR laser crystal will greatly simplify the manufacturing process for existing solid state laser systems such as microchip lasers and flashlamp pumped rod lasers. The crystals in these laser systems traditionally have a thin film mirrored coating deposited on opposite ends of the crystal to create a laser cavity, but the coatings are problematic, fragile, and expensive. A DFB structure placed inside the crystal will eliminate the need for mirrored coatings.

A DFB microlaser could have an impact on light sources used in telecommunications, medical display, military, and various other commercial applications. The telecommunications industry is moving towards wavelength division multiplexed (WDM) networks that require very stable, low noise laser sources. As the number of channels increase in WDM networks, the problem becomes more significant and special care must be used to prevent aliasing of the different laser sources. Even if a DFB microlaser was not used, a DBR mirror could be utilized to provide a stable feedback element for controlling the spectrum of diode lasers. A DFB microchip laser could also be advantageous in systems used for remote sensing of airborne contaminants for military field use, or emission

compliance for chemical processing plants that require narrow linewidth, stable, modest power, tunable light sources which are not cost prohibitive.

The medical community requires smaller Q-switched sources for microsurgery. A passively Q-switched DBF microlaser may be mounted on the end of an optical fiber to provide a local source of high peak power pulses in a small, elegant handheld device. By incorporating laser ions in a DFB media lacking a center of symmetry, such as $\text{Nd}^{3+}:\text{LiNbO}_3$, self-doubling or self-OPO devices can be constructed to make efficient visible light sources for projection displays or optical storage (Yakymyshyn).

Solid state lasers provide several advantages over diode lasers, including the ability to efficiently store optical energy and release it in controlled high peak power pulses, and the ability to generate output beams having exceptionally narrow optical linewidths, a low intensity noise, and a TEM_{00} diffraction limited transverse modal distribution. A successful demonstration of high quality distributed gratings in crystals or glassy materials will enable the creation of these devices.

Optical sensors have seen steady growth in the number of commercially successful applications over the past ten years (Dakin and Udd). Two of the most common barriers limiting the introduction of new optical sensors are sensor system cost and the sensor's ability to handle extremely harsh environments. Optical fiber Bragg gratings, for example, have difficulty competing with other technologies because of the costly need to couple light into single mode fiber. If DBR structures can be placed in bulk media, then bulk optical elements become feasible as sensor

elements in which the measurand is spectrally encoded by the reflectivity of the Bragg grating. Because of the use of a bulk material, multi-mode fiber and inexpensive light sources can be used as part of the sensor system, thereby lowering system cost. The sensing element can be a passive filter/reflector or an active laser whose lasing characteristics are modified by the environment. In addition, bulk monoliths can be extremely robust with proper material selection, permitting sensor use in traditionally untenable application areas such as metal foundries, down-hole oil and gas wells, jet engine and rocket engine manifolds, and radioactive waste containment vessels (Yakymyshyn).

The underlying hypothesis of this paper is the supposition that crystal growth techniques can result in the formation of precisely defined periodic variations in the refractive index in a crystalline or glassy monolith. These Bragg gratings will be characterized using scanning electron microscope cathodoluminescence (SEM CL) imaging and spectra, and SEM X-ray analysis and imaging. Optical diffraction will also be used to measure the pitch of the gratings to verify the SEM data. The final stage of this thesis will be to find and characterize any Bragg reflections.

CHAPTER 2

THEORY

Coupled Mode Theory

As mentioned before, distributed Bragg reflectors can have extremely high reflectance for a large number of interfaces. Because stringent phase requirements need to be met for the individual reflections to add, Bragg gratings are spectrally selective. The reflectance of a Bragg grating is typically solved using coupled mode theory, which is based on the assumption that the mode fields of an unperturbed waveguide remain relatively unchanged in the presence of weak perturbations.

The application of coupled mode theory (Yeh) assumes that the change in index of refraction is sinusoidal in nature. The index of refraction can be written as either

$$n(x) = n_0 + n_1 \cos(Kx), \quad (2-1)$$

or

$$n(x) = n_0 + n_1 \sin(Kx), \quad (2-2)$$

where n_0 is the average index of refraction of the material, n_1 is the depth of the modulation of the index, and K is the grating wave vector. K is related to the period of the index variation Λ by

$$K = \frac{2\pi}{\Lambda} \quad (2-3)$$

The depth of modulation is typically much smaller than the average index of refraction (i.e. $n_0 \gg n_1$). As an example, typical numbers for fiber Bragg gratings would be $n_0=1.46$ and $n_1=10^{-4}$.

With the index of refraction defined, it can now be used in the wave equation. The wave equation for light propagating along the x axis is given by

$$\frac{d^2}{dx^2} E(x) + \left(\frac{\omega}{c} n\right)^2 E(x) = 0, \quad (2-4)$$

where ω is the angular frequency and c is the velocity of light in a vacuum. By assuming that $n_0 \gg n_1$, and substituting $n(x)$ into the wave equation, the equation simplifies to

$$\frac{d^2}{dx^2} E(x) + \frac{\omega^2}{c^2} (n_0^2 + 2n_0 n_1 \cos Kx) E(x) = 0. \quad (2-5)$$

This differential equation can be solved using coupled mode analysis. The electric field can be expressed in terms of normal modes of the unperturbed structure, where the expansion coefficients depend on x . In other words, the solution to Eq. (2-5) can be written as the sum of a forward traveling plane wave (A) and a reverse traveling plane wave (B),

$$E(x) = A(x)e^{-ikx} + B(x)e^{ikx}, \quad (2-6)$$

where $\exp(-ikx)$ and $\exp(ikx)$ are the normal modes of the unperturbed structure.

The wavevector k is given by

$$k = \frac{2\pi n_0}{\lambda} = \frac{\omega}{c} n_0. \quad (2-7)$$

If $A(x)$ and $B(x)$ are constant, Eq. (2-6) is the general solution to the unperturbed case. $A(x)$ and $B(x)$ were made functions of x because with a perturbation (i.e. $n_1 \neq 0$), the modes $\exp(-ikx)$ and $\exp(ikx)$ are no longer the normal modes of the whole structure.

Begin the analysis by plugging the solution, Eq. (2-6), into the wave equation to obtain

$$\begin{aligned} A'' e^{-ikx} + B'' e^{ikx} - 2ikA' e^{-ikx} + 2ikB' e^{ikx} + \\ 2 \frac{\omega^2}{c^2} n_0 n_1 (A e^{-ikx} + B e^{ikx}) \cos(Kx) = 0, \end{aligned} \quad (2-8)$$

where a prime indicates a differentiation with respect to x .

This equation can be simplified further by assuming that the sinusoidal index variation is weak such that the variation of the amplitude is slow and satisfies the condition

$$|A''| \ll |kA'| \quad \text{and} \quad |B''| \ll |kB'|. \quad (2-9)$$

This condition is known as the parabolic approximation and is often used when perturbations are small. The simplified equation becomes

$$2ikA' e^{-ikx} - 2ikB' e^{ikx} = 2 \frac{\omega^2}{c^2} n_0 n_1 \cos(Kx) (A e^{-ikx} + B e^{ikx}). \quad (2-10)$$

To further simplify, both sides of the equation can then be multiplied by $\exp(ikx)$. By averaging, rearranging, and the realization that the sinusoidal and exponential are only significant when $2k \approx K$, the simplified equations can be written as

$$A' = -i \frac{\omega n_1}{2c} B e^{i(2k-K)x}, \text{ and } B' = i \frac{\omega n_1}{2c} A e^{-i(2k-K)x}. \quad (2-13)$$

The two differential equations can be further simplified by defining some constants.

The first one is a coupling constant given by

$$\kappa = \frac{\omega n_1}{2c} = \frac{\pi n_1}{\lambda}, \quad (2-14)$$

and the second is a phase mismatch term given by

$$\Delta\beta = 2k - K. \quad (2-15)$$

The final coupled equations can be written as

$$\frac{d}{dx} A(x) = -i\kappa B(x) e^{i\Delta\beta x}, \text{ and } \frac{d}{dx} B(x) = i\kappa A(x) e^{-i\Delta\beta x}. \quad (2-16)$$

The general solution for $A(x)$ can be found by multiplying both sides of the first equation by $\exp(-i\Delta\beta x)$ and then differentiating with respect to x . With some substitution and algebra, this method allows $B(x)$ to be eliminated and forms a second order differential equation. The general solution then becomes

$$A(x) = [C_1 \cosh(sx) + C_2 \sinh(sx)] e^{i(\Delta\beta/2)x}, \quad (2-17)$$

where C_1 and C_2 are arbitrary constants and s is given by

$$s^2 = \kappa^2 - \left(\frac{\Delta\beta}{2}\right)^2. \quad (2-18)$$

The term $B(x)$ can be found by simply rearranging the first equation in (2-16) and is given by

$$B(x) = \frac{i}{\kappa} e^{-i\Delta\beta x} \frac{d}{dx} A(x). \quad (2-19)$$

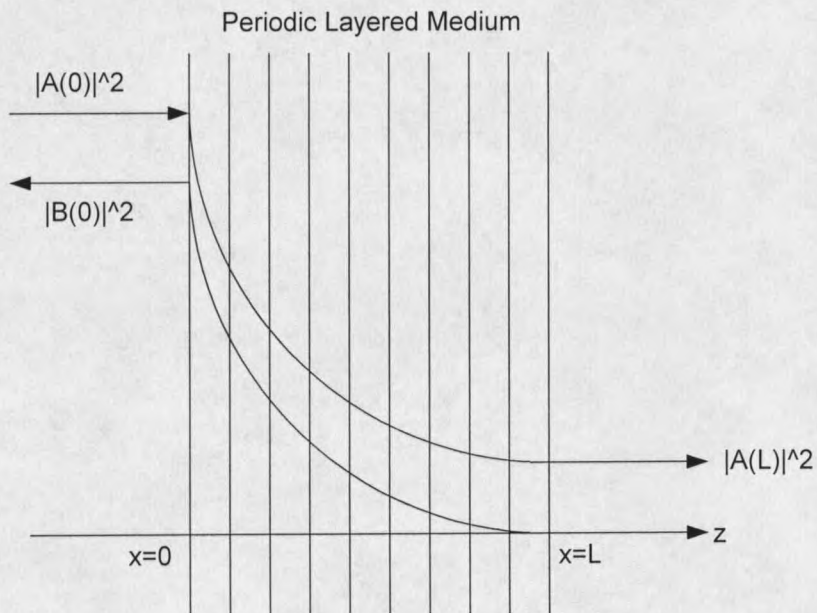


Figure 2-1: Mode powers of the incident mode ($A(x)$) and the reflected mode ($B(x)$) in a periodic layered medium when $\Delta\beta=0$.

With that complete, the reflection coefficient can now be found. Assuming the light is incident at $x = 0$, then the reflection coefficient can be written as

$$r = \frac{B(0)}{A(0)}. \quad (2-20)$$

Notice in Figure 2-1 that the number of layers is assumed to be large enough that the amplitude of reflected light at the end of the structure, $x = L$, will be zero. This means that at some certain wavelength, all of the light will be reflected and none of it will reach the end of the structure. Using these boundary conditions, the equations for $A(x)$ and $B(x)$ can be written as

$$A(x) = \frac{s \cosh s(L-x) + i(\Delta\beta/2) \sinh s(L-x)}{s \cosh sL + i(\Delta\beta/2) \sinh sL} A(0) e^{i(\Delta\beta/2)x},$$

$$B(x) = \frac{-i\kappa \sinh s(L-x)}{s \cosh(sL) + i(\Delta\beta/2) \sinh sL} A(0) e^{-i(\Delta\beta/2)x}. \quad (2-21)$$

Plugging Eq. (2-21) into the reflection coefficient equation gives

$$r = \frac{-i\kappa \sinh(sL)}{s \cosh sL + i(\Delta\beta/2) \sinh sL}. \quad (2-22)$$

From here, the reflectance can be found by taking the absolute square of r . The equation for the reflectance is finally given by

$$R = |r|^2 = \frac{\kappa^2 \sinh^2 sL}{s^2 \cosh^2 sL + (\Delta\beta/2)^2 \sinh^2 sL}. \quad (2-23)$$

The fractional power exchange into the reverse wave decreases as the value of $\Delta\beta$ increases. A complete power exchange into the reverse wave only becomes possible when the phase matching condition is satisfied at $\Delta\beta = 0$. Equation (2-23) then becomes

$$R = \tanh^2(\kappa L), \quad (2-24)$$

where there is a maximum power transfer only if $\kappa L \gg 1$, so that $\tanh(\kappa L) \approx 1$.

The phase mismatch term is the basis of a very important equation for designing Bragg gratings. This term can be rewritten as

$$\Delta\beta = 2k - K = \frac{4\pi n_0}{\lambda_0} - \frac{2\pi}{\Lambda} \quad (2-25)$$

When the phase matching condition is satisfied, the two expressions in Eq. (2-25) must be equal. Setting the two sides equal and rearranging gives

$$\Lambda = \frac{\lambda_0}{2n_0} \quad (2-26)$$

This equation gives the relationship between the pitch of a grating and the wavelength of light that will be reflected inside some medium.

Modeling

Mathcad. The equation for the reflectance can be used to model the reflectance versus wavelength of sinusoidal Bragg gratings. A program was written for this project in Mathcad (see Appendix A) to model the reflectance and to predict the performance of the crystal Bragg gratings.

The Mathcad program uses a slightly different equation than the one derived above. The equation that was just derived assumes the angle of incidence is zero, which simplifies the equation. The coupling coefficient and the phase mismatch term both depend on the angle of incidence. The equations change slightly to

$$\kappa(\theta_i) = \frac{\pi n_1}{\lambda \cos(\theta_i)}, \text{ and} \quad (2-27)$$

$$\Delta\beta(\theta_i) = \frac{4\pi \cos(\theta_i)}{\lambda} - \frac{2\pi}{\Lambda}, \quad (2-28)$$

where θ_i is the angle of incidence. The angle dependence causes the reflectance to shift to lower wavelengths with increasing angle.

The model was used to get an intuitive feel for the effects of changing various parameters. As the length of the crystal increases, there should be more reflected light at the Bragg wavelength because of the increase in the number of interfaces. An increase in the modulation depth should also increase the amount of reflected light because each interface has a larger index change.

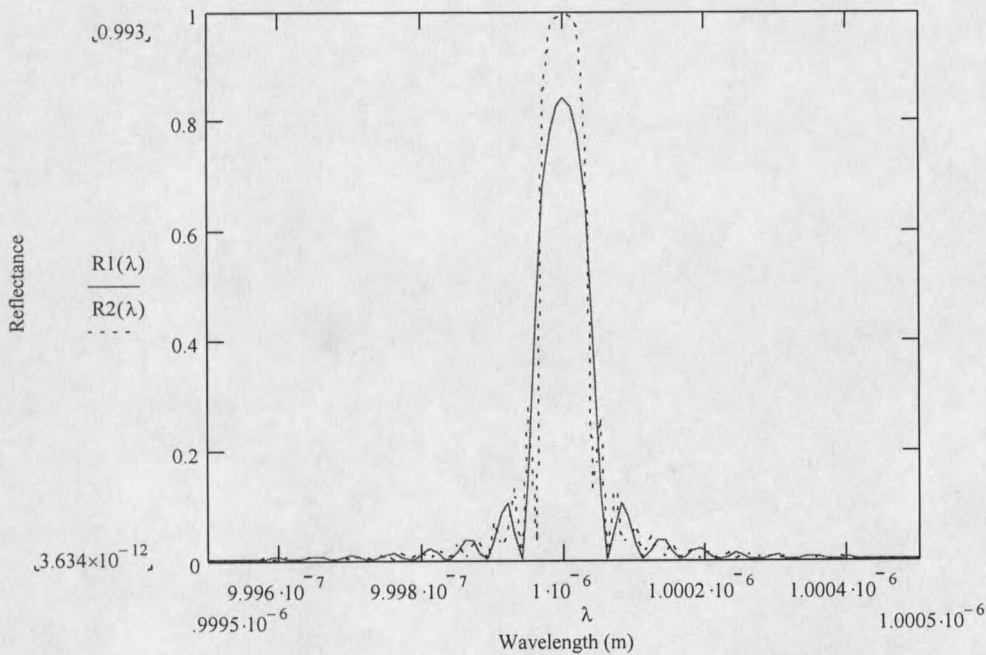


Figure 2-2: Reflectance from a 5mm and 10mm crystal.

The crystals were modeled under the assumption that the length of the crystal could vary between 5mm and 10mm. Due to the concentrations of the dopants inside the crystals, the modulation depth, Δn , was assumed to be

approximately $1\sim 2 \cdot 10^{-4}$. The exact pitch of the grating was inconsequential at this point. As shown in Figure 2-2, the reflectance changed from 0.84 to 1 using the assumed numbers where $R1(\lambda)$ was the reflectance from a crystal 5mm long with $\Delta n = 1 \cdot 10^{-4}$ and $R2(\lambda)$ was the reflectance from a 10mm crystal with $\Delta n = 1 \cdot 10^{-4}$. This showed that, at least theoretically, a crystal having either of the parameter sets, or anything in between, should have more than enough reflected signal to measure.

The length of the crystal is an easily changed parameter. The crystal could be fabricated with a bit more length. The depth of modulation is determined by the growth process, though this factor is not easily measured or controlled. Figure 2-3 shows another simulation with a 10mm crystal where $\Delta n = 1 \cdot 10^{-5}$. The reflectance has dropped considerably by changing the modulation depth. Changes in the grating growth process could generate smaller modulation depths.

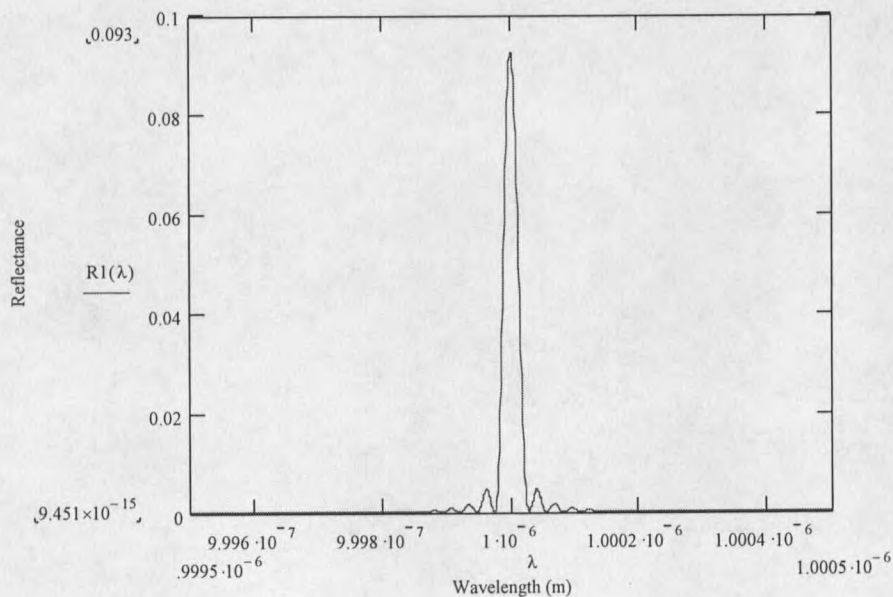


Figure 2-3: Reflectance from a 10mm crystal with a modulation depth of $1 \cdot 10^{-5}$.

Increasing the angle of incidence causes the light to have a different phase matching condition, and the result is a reflection at a lower wavelength. Figure 2-4 shows the reflectance from a crystal when the angle of incidence is 10° . The reflectance peak has shifted more than 52nm. This is a very large shift, but it is not too much of a problem for the paraxial case where the angles stay small. A 1° angle changes the wavelength by less than 0.2nm.

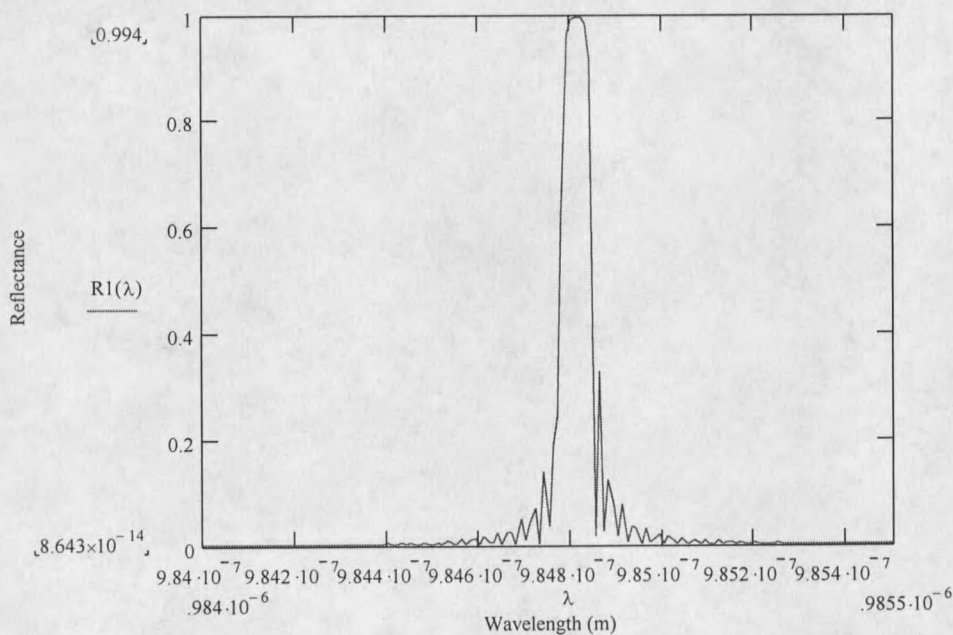


Figure 2-4: Reflectance from a crystal with a 10° angle of incidence.

Specview. Another program, Specview, was used to test the suitability of oxide crystals for temperature and pressure sensors. Specview is a commercial program primarily used to analyze in-fiber Bragg gratings. The parameters can be

set to model Bragg gratings in other materials, but there are a few limitations. The period of the grating is limited to between 100nm to 800nm. This range is fine to model reflections from the visible to near infrared, well within the telecommunications spectrum, but longer periods require the use of the Mathcad program. Specview also uses coupled mode theory to solve for the reflectance, but the program does not allow the angle of incidence to be changed. Specview does have some advantages over my Mathcad program. Material properties can be defined for crystals or optical fibers to account for temperature and pressure sensitivity. The pitch profile can be defined as uniform, linear, or arbitrary. Non-uniform gratings can then be modeled to examine the effect on the reflectivity. The index of modulation and modulation depth can also be set as either uniform, linear, gaussian, or arbitrary. The two programs gave similar results when the same parameters were used.

Table 2-1: Material Properties of $Y_3Al_5O_{12}$ (YAG).

Material Property	Value	Unit
Poisson Ratio	0.25	-
Photoelastic Coefficients	$P_{11}=0, P_{12}=0.019$	-
Thermal Expansion Coefficient	$7 \cdot 10^{-6}$	$1/^\circ\text{C}$
Thermo-optic Coefficient	$9 \cdot 10^{-6}$	$1/^\circ\text{C}$

Temperature and Pressure Model. Yttrium Aluminum Garnet ($Y_3Al_5O_{12}$), a very common oxide crystal, was modeled to discover if the material properties were suitable for temperature and pressure sensors. Table 2-1 shows a list of the material properties used. The other crystal parameters were a length of 10mm, Δn of $1 \cdot 10^{-4}$,

an average index of 1.83, and a pitch of 273.22nm to center the reflection at 1000nm.

Figure 2-5 shows the shift in wavelength due to changes in temperature. A 100°C change in temperature shifted the wavelength 1.6nm. This appears to be a linear shift with temperature because a change of 200°C shifts the wavelength 3.2nm, and this relation holds true for even higher temperatures. The applications for bulk media temperature sensors could make use of the extremely high melting points of oxide crystals (<2000°C) where the shift in wavelength could be easily measured. A sensor based on one hundred percent reflectance may not be the best choice for this type of application. Once the reflectance reaches the maximum, increasing the length or the modulation depth serves to broaden the reflected signal. It would be harder to see a shift in a wide spectral peak as opposed to the shorter widths of low reflectance signals.

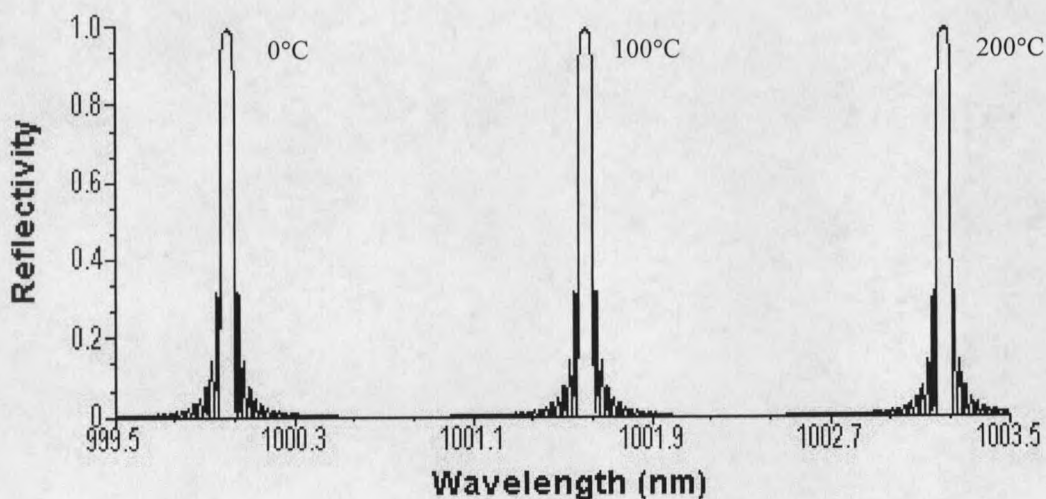


Figure 2-5: Reflectance from a Bragg grating in YAG at different temperatures.

Figure 2-6 shows the shift in wavelength due to pressure changes. The wavelength shifted only 0.013nm for an increase of 1000 PSI. The relation between pressure and wavelength is also linear. An increase in pressure of 2000 PSI shifted the reflected wavelength 0.026nm. This wavelength shift is very small, so YAG is not the best choice of material for a pressure sensor. The pressure differentials would need to be over 1000 PSI to have any hope of measuring pressure changes.

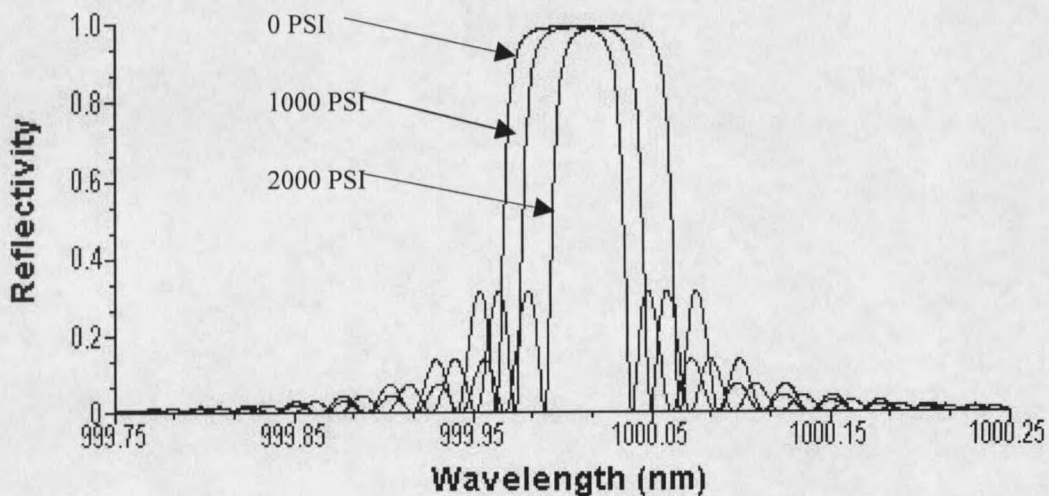


Figure 2-6; Reflectance from a Bragg Grating in YAG due to pressure changes.

CHAPTER 3

CZOCHELSKI GROWTH METHOD

The crystals were grown using the Czochralski growth method, which is used to grow oxide crystals like Yttrium Aluminum Garnet (YAG) and ruby. The elements of the oxide crystals start in a powdered form. The powders are mixed and placed in an iridium crucible, which is chemically inert. The crucible is inserted into an induction furnace. An induction furnace is used because it can safely generate the high temperatures needed to melt the powders. When the powders are finally melted and temperature reaches the right point, a seed crystal is dropped into the melt. The seed crystal is rotated and slowly pulled from the melt. This produces a crystal boule that can be cut up to fabricate laser crystals or oxide filters, windows, and lenses. Figure 3-1 shows a schematic of a Czochralski induction furnace.

The crystals are typically doped with laser active species. These doped crystals form the foundation of many solid state lasers. The pull rate, rotation speed, and temperature of the melt all affect the concentration of the dopants. Typical growth runs try to keep these three factors as constant as possible. This creates an optically clear crystal with a uniform dopant concentration across most of the boule. Fluctuations can cause local variation in the dopant concentration called striae. In regular laser crystals, the formation of striae is a major problem.

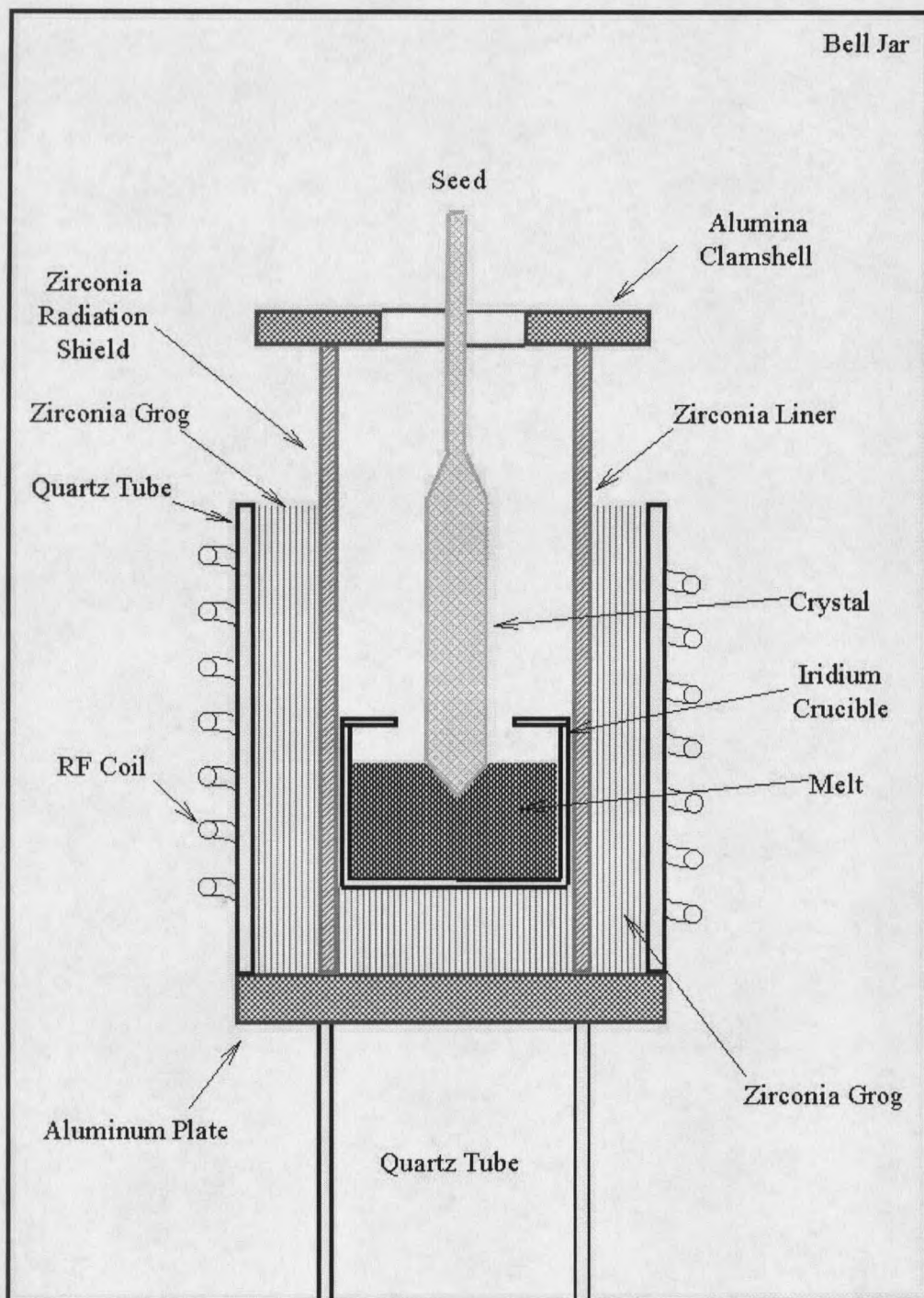


Figure 3-1: Schematic of a Czochralski Furnace (Courtesy of Scientific Materials Corp.).

Periodic Striae

Scientific Materials Corp. has perfected their growth method to produce extremely pure crystals with no striae. In the process of eliminating striae, they have discovered methods to introduce periodic striae. This is the basic premise upon which this thesis is based. The periodic striae act like a Bragg grating by causing localized index variations due to the change in dopant concentration. In DFB applications, the dopant variation also causes a periodic fluctuation in the gain.

Off Thermal Center. There are a couple of different methods being used to introduce periodic striae in the crystals. The first method involves placing the seed crystal off thermal center. There is a temperature gradient across the crucible: the melt is hottest at the walls of the crucible, and it cools towards the center of the crucible. Normally the seed crystal is placed in the middle of the crucible on thermal center to keep the temperature gradient constant across the surface of the crystal/melt interface. Placing the seed crystal off center causes a periodic temperature variation as the crystal rotates. The dopant concentration increases with increasing temperature. This effect has been seen in a CTH:YAG crystal. CTH:YAG is a YAG crystal doped with the laser active species Chromium (Cr^{3+}), Thulium (Tm^{3+}), and Holmium (Ho^{3+}). The first crystal to show a periodic variation in the dopants was crystal 1-525B. This effect was completely unintentional, but since then CTH:YAG crystals have been grown with the express purpose of introducing striae. The crystal growers have a hard time controlling the

striae using this process. The striae may be very uniform, but the pitch will be uncertain due to the lack of a method to directly measure how far the seed crystal is off thermal center. Models of the crucible and growth chamber can predict the temperature off thermal center, but measurements of the temperature gradient in the melt cannot be accurately made.

Varied Pull Rates. The next few methods involve more controllable growth procedures. The pull rate and rotation speed are controlled by programmable microcontrollers. The growth run can then be conducted either manually or by a set program. Striae have been grown in CTH:YAG using three different programs. The first program pulls the crystal at two different rates. The slower pull rates give the dopants more time to diffuse into the crystal. The second program starts and stops the pull rate. This should have the same effect as the adjacent pull rate, but with much larger discontinuities in dopant concentrations. The third program periodically adjusts the rotation speed. Table B-1 in Appendix B lists all of the crystals grown to date for this project.

CHAPTER 4

EXPERIMENTAL SETUPS AND RESULTS

Scanning Electron Microscope

The samples were polished and prepared for the SEM by cleaning them in ultrasonic baths of acetone, methanol, and hexane. The sample surface to be imaged was coated with a conductive layer of carbon to dissipate electrostatic charging. A thin layer of carbon was required to minimize optical absorption of the CL light generated by the sample while maintaining sufficient electrical conductivity to dissipate static charge. Several different methods were used to characterize the samples. The first involved imaging the largest surface of the sample using CL over the visible and near infrared to verify the existence of striae and measure the pitch. For the second method, a monochromator, placed between the collection optics and the PMT (photo-multiplier tube), was set at several discrete emission wavelengths and the resulting SEM CL image was recorded to determine if the striae were correlated with a particular laser active species in the YAG host. The third method involved making x-ray point measurements and x-ray imaging maps to determine which laser active species were responsible for the observed striae.

Cathodoluminescence. A typical SEM CL image of sample 1-525B is shown in Figure 4-1. The striae are clearly visible, although the period varies considerably, even over the relatively small aperture shown in the image.

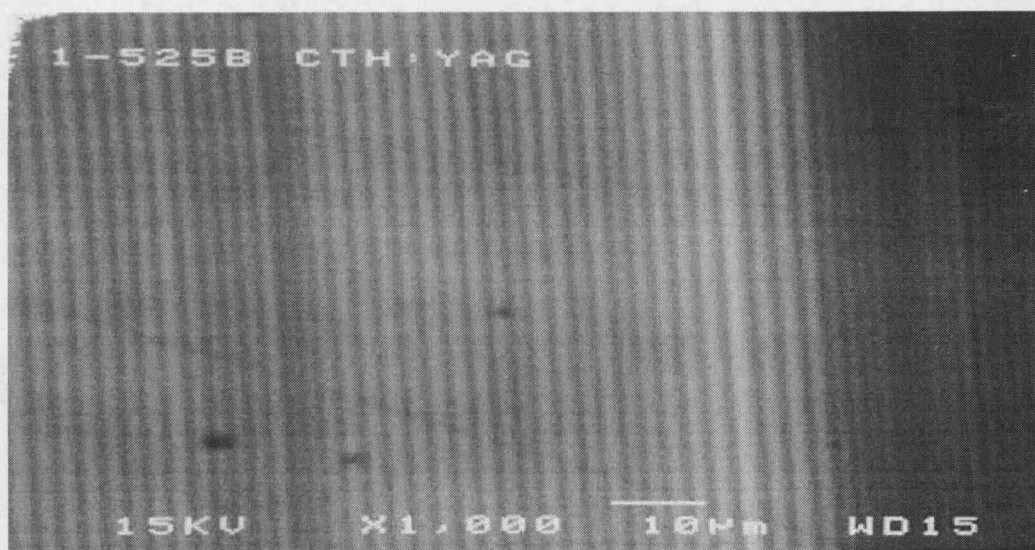


Figure 4-1: SEM CL image of sample 1-525B showing structured, broadband CL emission.

The CL emission shown in Figure 4-1 was gathered using the monochromator in a polychromatic setting. This setting did not restrict the CL emissions to a specific wavelength.

A CL emission spectrum was gathered from $0.2\mu\text{m}$ to $0.8\mu\text{m}$ with the monochromator in the monochromatic setting. The monochromator scan was performed in 2nm increments. The emission spectrum for sample 1-525B, shown in Figure 4-2, exhibits many emission peaks. Three main peaks can be seen around 362.77nm, 470.39nm, and 716.58nm.

There were many different emission peaks due to the various laser active species in the crystal. To try and identify the individual species generating each of the emission peaks, samples of $\text{Ho}^{3+}:\text{YAG}$ (3-5), $\text{Cr}^{3+}:\text{YAG}$ (9-41), and $\text{Tm}^{3+}:\text{YAG}$

(10-28) were fabricated. Optical spectra were generated for each of the crystals. The three optical spectra were used to interpret the CTH:YAG spectra. The 362nm and 470nm peaks were due mostly to Thulium³⁺. The 715nm peak was due to the Chromium³⁺. The Holmium³⁺ gave a very weak emission and contributed very little to the emission spectrum for CTH:YAG.

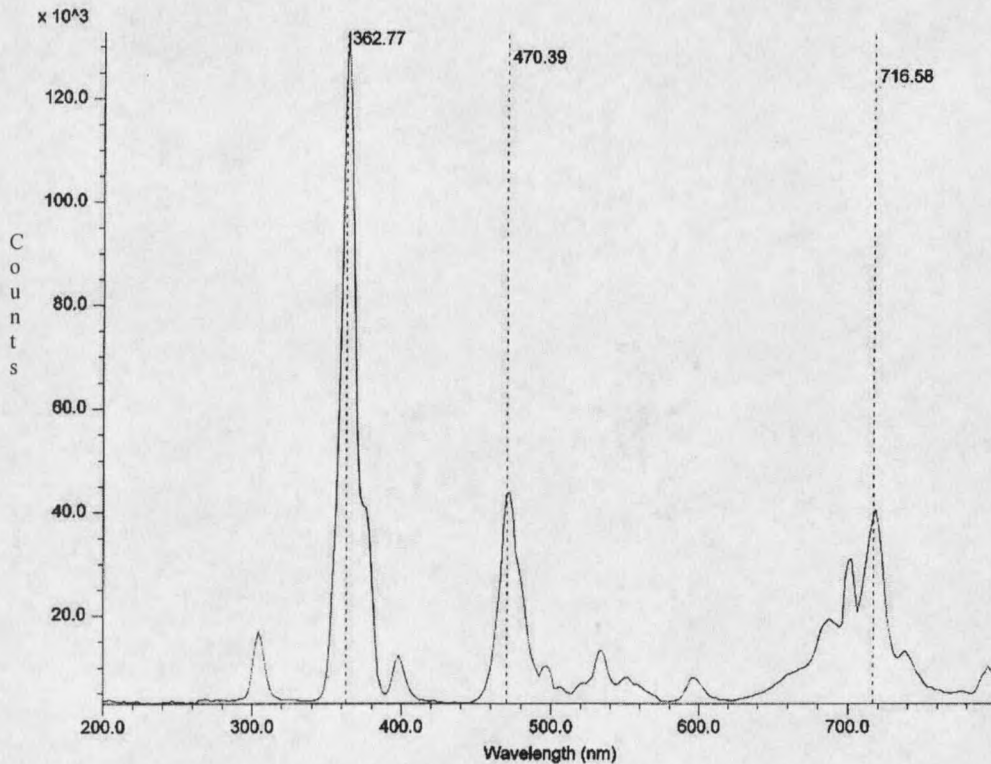


Figure 4-2: CL emission spectrum for sample 1-525B, CTH:YAG.

The monochromator was set at the three main emission peaks to take CL images at those wavelengths. The CL images are shown in Figures 4-3, 4-4, and 4-

5. All three of the images show a periodic structure, but the contrast ratio is very poor at 716.6nm. Based on these images, it was concluded that the majority of the emission intensity for the periodic structure came from the emission peaks at 362nm and 470nm. Therefore most of the SEM CL signal appears to result from emission from the Thulium ion.

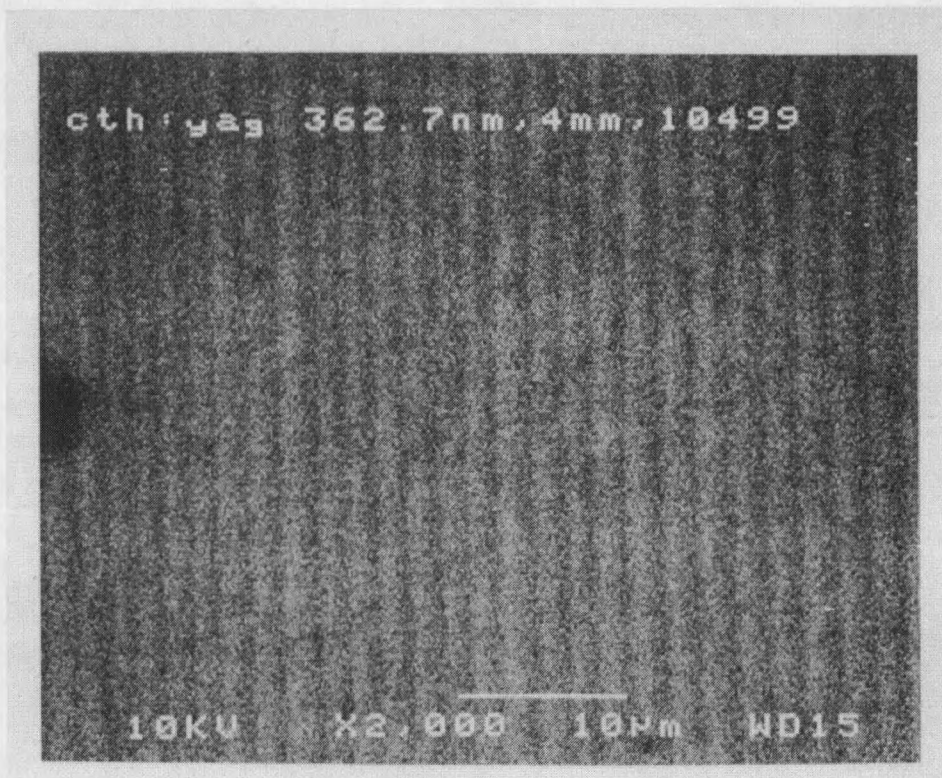


Figure 4-3: SEM CL image from CTH:YAG sample 1-525B at a detection wavelength of 362.7nm.



Figure 4-4: SEM CL image from CTH:YAG sample 1-525B at a detection wavelength of 470.4nm.

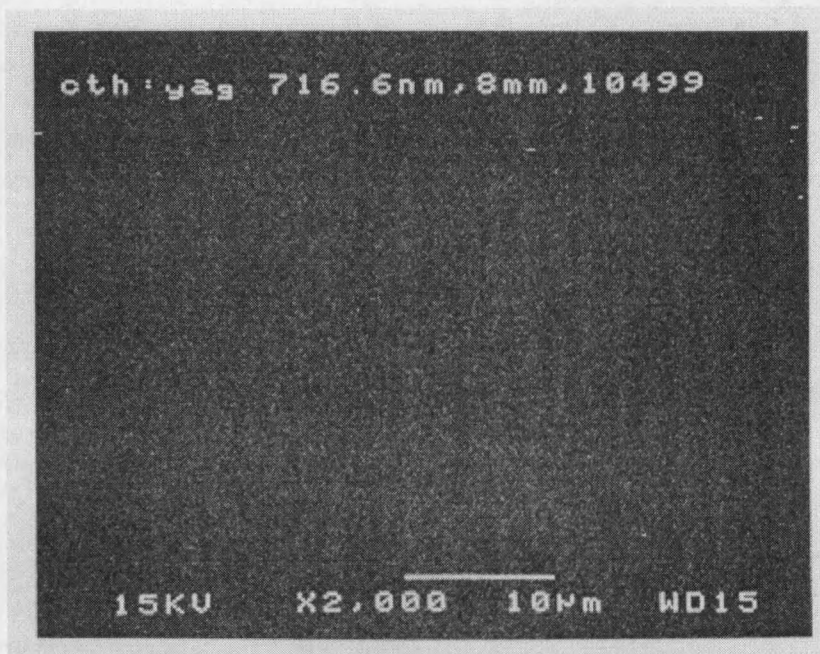


Figure 4-5: SEM CL image from CTH:YAG sample 1-525B at a detection wavelength of 716.6nm.

Five of the samples fabricated for this project were imaged with broadband SEM CL. A summary of the SEM CL measurements follows;

- a) 2-526 3 μm showed a uniform periodic structure of 2.5 μm .
- b) 2-526 2 μm showed non-uniform striae of 3 to 5 μm .
- c) 2-527 Top showed a uniform periodic structure of 1.67 μm .
- d) 2-527 Mid showed wildly varying striae averaging 3 μm .
- e) 2-527 Bottom showed wildly varying striae averaging 5 μm .

The two remaining crystals, 2-526 1.5 μm and 2-526 1.064 μm , were not imaged. These two samples were grown with designed grating periods of 0.4 μm and 0.29 μm , respectively. These striae periods were assumed to be too small to be effectively imaged, since the SEM CL imaging technique has a lateral resolution that is limited by the scattering range of electrons once they enter the sample surface. The maximum range for electrons having energies of 1 – 20 keV is given empirically by [Feldman and Mayer]

$$R(\mu\text{m}) = 0.064(E_0)^{1.68} / \rho \quad (4-1)$$

where R is the electron range in the solid in microns, E_0 is the incident electron energy in keV and ρ is the mass density of the sample in gm/cm^3 . For typical values of $E_0 = 15$ keV and $\rho = 4.55$ gm/cm^3 for undoped YAG, the electron range is $R=1.33$ μm . Since excitation of CL requires very little electron energy (typically <10 eV), the CL volume is expected to closely correlate with the electron range. Since emission extends over 4π steradians, the actual range of optical signal

generation is expected to be slightly larger than the electron range in the solid. This range will likely prevent any imaging of striae finer than 1 μm when using an electron beam energy of 15 keV. To improve the lateral resolution of SEM CL, the beam energy can be lowered at the expense of decreased signal and decreased signal to noise ratio. For example, reducing the electron beam energy to 5 keV will give a calculated electron range of 0.21 μm , permitting the imaging of striae of this size. Images of sample 1-525B confirmed that the image sharpness was improved when the beam energy was reduced from 15 keV to 5 keV. However, the scan time was increased by a factor of ten to generate enough signal for a quality image. This will become more challenging as smaller striae pitches are imaged. Still, it appears in principle that we could successfully image striae having pitches of 0.2 – 0.3 μm using SEM CL.

X-ray Analysis. X-ray spectral analysis was performed on crystal 1-525B. X-ray analysis is used to determine the atomic percent composition of a sample. By examining the elemental composition at two points corresponding to light and dark bands in the SEM CL image, it was hoped that the differences in CL emission intensity could be correlated with atomic percent variations of the dopants in the crystal. This approach was complicated because the SEM setup was quite different for CL analysis and x-ray analysis. The process involved finding an imperfection on the surface of the crystal and then looking at the CL image of that area. Once the imperfection was determined to be on a dark or bright band, then the x-ray analysis was performed on that same spot. The data showed that the bright and

dark bands do have a variation in the dopant concentrations. The variations were on the order of a few percent. Unfortunately, it was hard to be absolutely certain that alternating bright and dark bands were analyzed. The results of this experiment were inconclusive.

The SEM is also capable of performing x-ray imaging. An x-ray image provides a two-dimensional color plot of the local atomic percent of a particular elemental species in the sample. An attempt was made to create an x-ray image of sample 2-526 (3 μ m). The imaging was performed with a 128x128 pixel sampling field and a one second dwell time at each pixel. There was no perceptible contrast in the resulting image that correlated with the SEM CL images taken on the same sample. A second attempt at an x-ray image using ten second pixel dwell times (the maximum allowed for x-ray imaging with this machine) was still inconclusive. This dwell time may still have been inadequate, since the pixel dwell time used for single point x-ray analysis was over two hundred seconds. The pixel field was then reduced to a single line of one hundred elements. In this mode, the maximum ten second pixel dwell time was used, but an additional averaging was performed by averaging one hundred line scans. Unfortunately, the line image results were still inconclusive. It was concluded that x-ray imaging was not a suitable tool for these samples.

Optical Characterization

Optical quality, polished samples of doped YAG were fabricated. The rectangular parallelepiped-shaped 5 mm x 5 mm x 10 mm samples were oriented

such that the grating structures were nominally parallel to the smallest face of each sample. The large faces allowed observation of the edge of the grating structure using SEM CL in the visible and near infrared spectral regions.

Since a periodic variation of the dielectric constant inside a bulk crystal can give rise to Bragg diffraction, broadband light incident at near normal incidence to the periodic structure in the crystal will result in a contradirectional, specular reflection for a very narrow range of wavelengths. The remaining light spectrum passes unaffected through the crystal. The reflected free-space wavelength, λ , of light is related to the pitch, Λ , of the periodic structure and the average refractive index, n , of the crystal by

$$\Lambda = \frac{\lambda}{2n}. \quad (4-2)$$

Optical measurements were used to verify this relationship in the fabricated samples. Several approaches were used to measure, or attempt to measure, the pitch by probing the spectral behavior of the samples. The resulting calculated pitch was then compared with the pitch derived from SEM CL images.

Although initial SEM CL measurements indicated the presence of strong grating structures, the actual pitches were approximately $2.5 \mu\text{m}$. With a refractive index of 1.82, the predicted first-order Bragg reflection occurs at a wavelength of $9.15 \mu\text{m}$. The transparency window for undoped YAG extends only to $6 \mu\text{m}$, preventing the direct observation of Bragg reflections from these samples. If the grating structure is not purely sinusoidal in shape, a fine structure factor for the grating can lead to higher order diffraction terms at shorter wavelengths, which is in

direct analogy to the fine structure function used in conventional X-ray diffraction theory. Thus, in principle, if a highly non-sinusoidal grating can be made, then the Bragg backreflection can be observed at a number of shorter wavelengths that lie within the transparency window of the YAG host crystal.

Optical Spectrum Analyzer. To allow optical characterization of the periodic structures, two approaches were attempted. In the first approach, a collimated broadband optical beam (either white light or a surface emitting Light Emitting Diode) was incident on the crystal, and backreflected light was collected by the same collimating optic. Figure 4-6 shows the setup using an HP70004A optical spectrum analyzer connected to the backreflection arm of a 50/50 fiber optic coupler that was used to detect any backreflections at specific wavelengths. Angle-polished fiber optic connectors were used to minimize Fresnel backreflections at the connector ferrules. Because the setup was only sensitive to 800 – 1700nm wavelengths, the non-sinusoidal nature of the periodic structures needed to be strong enough to generate a higher order Bragg reflection (5th or 6th order). This approach did not produce any detectable reflection peaks.

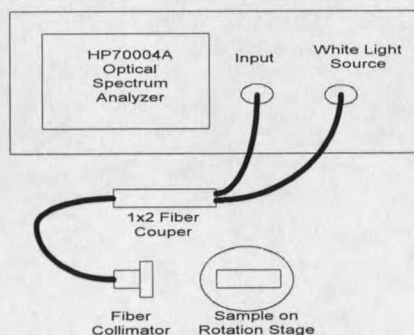


Figure 4-6: Optical spectrum analyzer backreflection experimental setup.

Optical Diffraction. The second approach borrows from acousto-optic interactions between acoustic and optical fields in a bulk medium. A bulk Bragg grating seen from the side (i.e. at an angle of incidence of $\pm 90^\circ$) looks like a bulk diffraction grating with the same pitch. When this configuration is used, the pitch of the grating and the wavelength of diffracted light are related by

$$\Lambda = \frac{q(\lambda/n)}{\theta} \quad (4-3)$$

where Λ is the pitch, λ is the free-space wavelength, n is the index of refraction, q is the order number (± 1 in this case), and θ is the (small-angle) angle of diffraction in the crystal. With this approach, shorter optical probe wavelengths result in smaller diffraction angles, permitting the characterization of long-period structures with visible wavelength light.

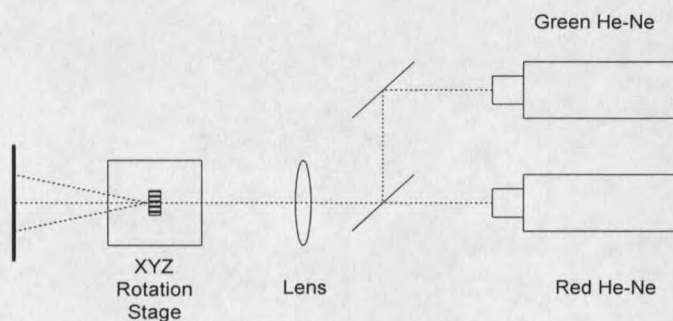


Figure 4-7: Small-angle diffraction experimental setup.

Figure 4-7 shows the experimental setup used to make small angle diffraction measurements. The unpolarized collimated output of a visible red (632.8nm) or green (543.5nm) He-Ne laser was focused by a 10-cm focal length plano-convex lens onto the sample. The sample was mounted on a three-axis

translation stage equipped with two additional rotational degrees of freedom. The resulting beams exiting the sample were propagated through free space and illuminated a scattering surface 10 - 20 cm from the sample. The resulting optical image on the scattering surface was digitized or sampled with an optical power meter to record intensity versus displacement from the undiffracted optical beam. The two He-Ne laser wavelengths were used to investigate the wavelength dependence of the diffracted patterns on the screen. Based on the geometry of the setup, the external diffraction angle was calculated. From this the internal diffraction angle was inferred for comparison with the expected diffraction angles based on the pitch measured using SEM CL.

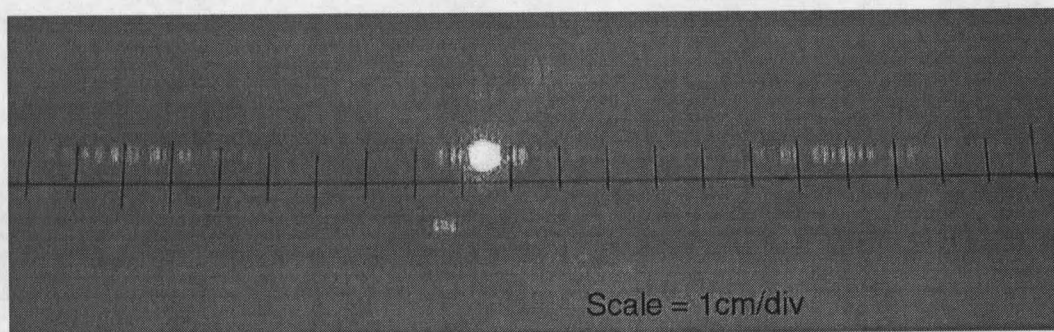


Figure 4-8: Diffraction pattern at 543.5nm from sample 1-525B.

The first crystal placed in the setup was crystal 1-525B. This crystal showed a strong optical diffraction pattern. A sample of the diffraction pattern measured with the green He-Ne laser is shown in Figure 4-8.

Although the image in Figure 4-8 is representative of the diffracted images observed, significant variations in the detailed structure of the diffracted image as

well as large variations in the intensity of the diffracted light were observed as different parts of the sample were probed with the incident optical beam. In addition, the diffraction into the $\pm 1^{\text{st}}$ order was composed of a series of spots rather than a single bright spot. There was also a significant amount of diffracted light near the zero-order beam at the center of the image in Figure 4-8. The structure seen was due to the presence of irregularities in the period of the grating structure present in the sample. The variations were consistent with the SEM CL images taken of this sample (see Figure 4-2), which showed large variations in the pitch even over a total image area of only $100 \mu\text{m}$.

The external diffraction angle for sample 1-525B at 632.8nm wavelength was calculated based on a 27-cm distance between the screen and the crystal sample. Using a distance of 7.3 cm from the undiffracted spot to the brightest first order spot measured on the screen, the resulting external diffraction angle for this sample was 15.13° (0.264 radians). The internal angle was then found using Snell's law to compensate for refraction at the exit surface of the crystal. The resulting internal diffraction angle was 8.1° (0.141 rad). Using Equation (4-3), the period of the grating structure in the sample was found to be $\approx 2.4 \mu\text{m}$. This result is in excellent agreement with the pitch of $2.3 - 2.5 \mu\text{m}$ measured using the SEM CL technique.

This measurement represents the first verification that the periodicity detected using the SEM CL technique is consistent with the presence of a periodic variation in the refractive index of the grating.

Several additional measurements were made with the setup shown in Figure 4-7. One involved measuring the angle required to achieve TIR (Total Internal Reflection) at the exit surface of the sample. The sample was first rotated until the diffraction pattern was symmetric about the undiffracted beam position. By rotating the sample on either side of this reference angle and comparing the rotation angles needed to achieve TIR, the tilt of the grating relative to the physical surfaces of the sample could be determined. For sample 1-525B, the reference angle was 230° . The angles required to achieve TIR were 223.5° and 253° . The angle differences were -6.5° and $+23^\circ$. This showed the grating was mis-aligned with the edges of the crystal by approximately 8° . This was a reasonably good result considering the initial assumption that the grating forms at the growth interface in the melt, and the difficulty in determining the precise growth interface angle.

The diffraction efficiency of the grating was also measured by summing the optical power in each of the first order diffracted regions. A power meter head was swept across the diffraction pattern next to the screen and the detected powers were recorded and summed. The efficiency was calculated as the sum of the power in the first order spots divided by the power in the zero order spot. For sample 1-525B, the diffraction efficiency was about 0.67%:

The diffraction efficiency of sample 1-525B was compared with the diffraction efficiency calculated based on a periodically varying refractive index profile. The diffraction efficiency for small-angle acousto-optic interactions [Yariv and Yeh] was adapted to the present case. The diffracted intensity is given by

$$\frac{I_{diff}}{I_{incident}} = \sin^2(\kappa L) \quad (4-4)$$

where the coupling constant κ is given by

$$\kappa = \frac{\pi \Delta n}{\lambda_o \cos \theta_{Bragg}} \quad (4-5)$$

and Δn is the refractive index modulation, λ_o is the vacuum wavelength of light, and $\cos \theta_{Bragg}$ is the Bragg diffraction angle. These relationships assume that the Bragg condition is satisfied. Using the total diffracted intensity for sample 1-525B, the coupling constant is approximately 20 m^{-1} (assuming an interaction length in the crystal of 5 mm and a small ($<20^\circ$) Bragg angle), giving a refractive index modulation depth of $\Delta n = 4 \times 10^{-6}$. This is much smaller than the values of $1 - 2 \times 10^{-4}$ expected if the dopant atom concentrations were being modulated by 1-2 wt.%. The differences are at least partly due to the long interaction length assumed in the calculation. The optical spot size was approximately 0.5 mm, and it was not clear if the Bragg condition was satisfied in the experimental setup used to measure total diffracted intensity. However, the fact that the diffraction efficiency is so low indicates that the dopant concentration modulation in this sample was not sufficient to create a large refractive index variation on a micron scale. It should be noted that much larger refractive index variations can be observed near absorption features of the dopant atoms, the concentrations of which are being spatially modulated. The wavelength dependence of the diffracted intensity was not investigated in this study.

2mm and 0.5mm thick samples were fabricated from the crystal boule 1-525B to make diffraction efficiency measurements. The diffraction efficiency of the 2mm crystal was about 0.168%. There were no diffracted spots from the 0.5mm thick crystal. This means that the diffraction efficiency depends on the crystal length so the Δn measurements reported above should be relatively accurate.

The measurements were repeated at a second wavelength to verify that the detected spots were indeed due to optical diffraction in the bulk sample, and not due to surface scatter or other defects in the sample. Because the experimental setup was altered, a different region of sample 1-525B was used for the diffraction measurements. At 632.8nm, an external diffraction angle of 16.5° resulted in a grating pitch of $2.15\mu\text{m}$. At 543.5nm, an external diffraction angle of 25.9° resulted in a grating pitch of $2.14\mu\text{m}$. These two measurements are in excellent agreement, and they provide evidence that the diffraction equation (4-3) is valid for these grating structures.

As part of this project, several crystal growth runs were completed and samples created for SEM CL and optical characterization. Appendix B gives a list of all of the crystals fabricated for this project. Because the CL spectra showed that the striae was due mainly to the Thulium, three samples were prepared from a growth run of 4% Tm:YAG (Crystal 4-418). None of these crystals produced an optical diffraction pattern nor displayed any periodic structures using the SEM CL imaging. Three samples were prepared from a growth run of 5% Tm:YAG (Crystal 2-559). The diffraction measurements produced periodic diffracted light around the

zero-order spot that has been characteristic of the crystals with striae, but there were no observable first order spots. The SEM CL imaging did not display any obvious striae.

More CTH:YAG crystals were made because they seemed to reliably produce periodic striae. The next four samples (Crystal 2-526) were grown with the intention of introducing grating pitches that would produce reflectance peaks at 3 μm , 2 μm , 1.5 μm and 1.064 μm . The zero order diffraction was visible on all of the crystals, but the first order diffracted spots could only be seen on one crystal (2-526-3 μm). The diffraction pattern was very faint; therefore, only the angle of diffraction was measured. The internal angle of diffraction was 7.67° , giving a pitch of 2.54 μm . This result agreed with the CL imaging, but was far from the desired pitch of 0.833 μm needed to provide an optical reflection peak at 3 μm .

Three more samples of CTH:YAG (Crystal 2-527) were made using different growth conditions to introduce a Bragg grating. All three crystals were grown with the hope of creating a pitch that would have a reflectance peak of 2.5 μm (a physical pitch of 0.67 μm). Of these three crystals, only one crystal produced a diffraction pattern. Crystal 2-527 Top had an internal angle of diffraction of 12.4° , giving a pitch of 1.57 μm and a potential reflectance peak at 5.84 μm . With this particular growth run, a small hole in the crucible created an uncontrolled loss of melt volume and a wild variation in grating period with position. This run was repeated with a new crucible and growth station. The three samples (2-537) were darker than the other CTH:YAG crystals due to a

contamination of calcium. These new crystals had the zero order structures, but no first order spots. The CL imaging produced no visible striae.

Two final growth runs were made during the time frame of this project. The first set of three crystals (10-206) were made by adjusting the pull rates. These three crystals all produced the zero order structure, but again, no first order spots or good CL images were collected. The zero order structures in the crystals indicate the presence of a periodic structure, but the modulation in the index of refraction may be too small to create strong diffraction patterns or good CL images. The final three crystals (2-561) were made by placing the seed crystal off thermal center. These three crystals all produced first order diffraction spots. The spots were very faint, but the diffraction angle measurements could still be made. The first order spots had broad structures indicating a non-uniform pitch. The pitches were calculated using measurements to the brightest point in the first order spots. Crystal 2-561 Top, Middle, and Bottom had calculated pitches of about $1.25\mu\text{m}$, $1.45\mu\text{m}$, and $1.3\mu\text{m}$ respectively. Only crystal 2-561 Bottom showed striae using CL imaging. Even using the longest scan time, changing the electron beam acceleration voltage, and adjusting the brightness and contrast, the resultant image produced barely visible striae. The pitch of the observable striae corresponds well with the diffraction calculation pitch.

As the grating period is reduced to achieve reflection peaks within the transmission band of YAG, a problem arises in the diffraction angle measurement setup. If crystals are grown with optical reflectance peaks of $3\mu\text{m}$ and lower, the

internal angle of diffraction can be greater than the angle for total internal reflection at the exit surface of the sample. The diffracted light will undergo multiple reflections in the crystal and be scattered or refracted out of the crystal at an unexpected angle. A white YAG cylindrical lens was fabricated and an index-matching solid was acquired to provide an index-matched interface between the sample exit surface and the optically contacted lens. The cylindrical exit surface of the lens should prevent TIR from occurring and allow visualization of the diffracted beams.

Bragg Reflection Measurements

Many of the crystals were grown with pitches that yield Bragg reflections in the deep IR. Conventional methods of measuring Bragg reflections could not be used for the project due to the wavelength range. If crystals are grown with pitches that result in first order Bragg reflections in the near IR (800nm – 1700nm), then the optical spectrum analyzer setup described above could be used.

Two different stations were assembled to make measurements out to 6 μ m. The limit of 6 μ m was chosen because YAG is optically transparent up to that wavelength. As shown in Figure 4-9, after 6 μ m there is a drastic cutoff in the transmission of IR energy. Even if longer wavelength light could make it far enough into the crystal to be reflected, the reflected signal would be absorbed before it could be measured.

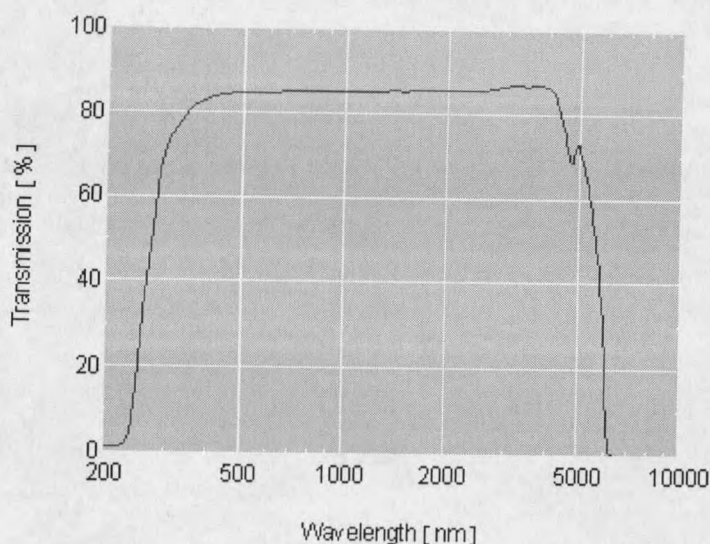


Figure 4-9: Transmission window of YAG.

Real Time Scanning Monochromator. The first setup was designed to continuously scan a small set of wavelengths over a span of $2\mu\text{m}$ and $6\mu\text{m}$. The setup works on the same principle as a monochromator. A monochromator is a variable wavelength filter. Broadband light passes through an entrance slit and is reflected off a diffraction grating. A small portion of the diffracted light will make it through an exit slit. Since different wavelengths of light will diffract at different angles, the wavelength selectivity depends on the position of the diffraction grating with respect to the slits. The width of the slits determines the linewidth of the output signal.

The first setup utilized the same principle, but the crystal sample was placed in the beam path between the entrance slit and the diffraction grating. The light source was a heating coil that could be thought of as a blackbody IR source. The IR radiation passed through a slit and was focused onto the crystal sample. In the beam path was placed a beam chopper and a 50/50 beam splitter. The significance

of the chopper will be discussed in a moment. The beam splitter was used to redirect a reflected signal from the sample back into the system. Once the beam was reflected it was diffracted using a diffraction grating. The diffraction grating was mounted on a galvanometer that allowed the grating to be continuously swept through a small range of angles. The diffraction grating and galvanometer were placed on a rotation stage so that the system could sweep between 2 and 6 μm . The diffracted light was collected with a lens and then focused through a slit onto a TE-cooled IR detector (HgCdZnTe 2-6 μm). Because the signals reaching the detector were very small, the output of the detector was passed through a preamplifier (SRS SR560), a lock-in amplifier (SRS SRS10), and finally displayed on an oscilloscope.

Figure 4-10 shows the layout of the system.

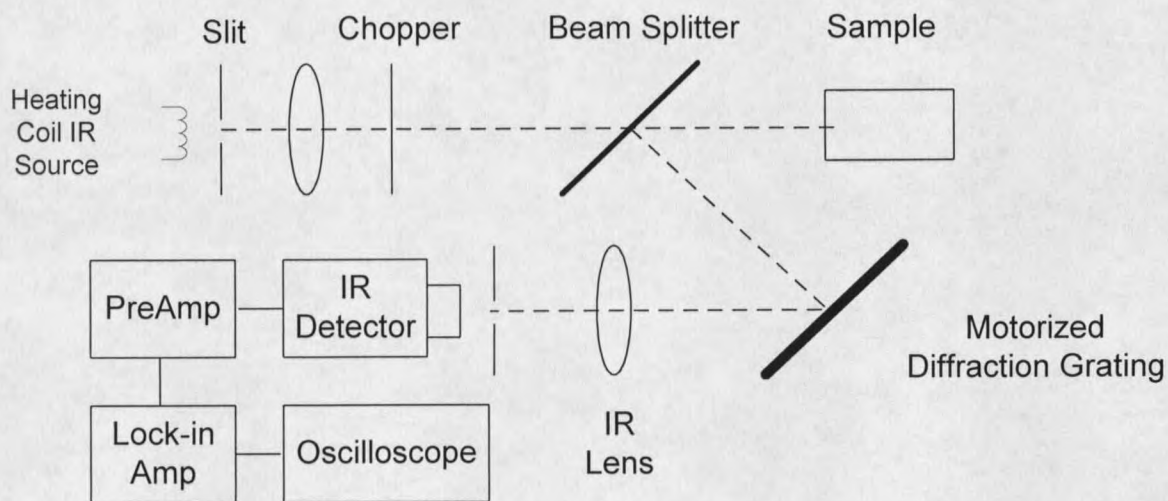


Figure 4-10: Layout of the first reflectance station.

There were two reasons why a chopper was used in this setup. The detector was only sensitive to AC signals, so the continuous source needed to be chopped.

The chopper was connected to the lock-in amplifier. This increased the signal to noise ratio of the system because the lock-in amp was only sensitive to signals that were at the frequency of the chopper and did not amplify DC background noise.

The system was aligned and calibrated using various IR narrow band pass filters (NBPF) at 2300nm, 4550nm, 5750nm, and 6075nm placed in front of the test sample, a gold mirror.

This station had a number of inherent problems. The IR source put out only a limited amount of IR energy, but the physical layout of the system required the IR radiation to be attenuated twice by passing through the 50/50 beam splitter. With 100% reflection from the sample, only 25% of the original energy would be directed towards the diffraction grating. There was also a trade off to be made between the path length and the divergence of the beam. There were minimum path lengths governed by the physical sizes of the components and the focal lengths of the lenses. If the focal length of the lens was too short, the beam would diverge too quickly and most of the reflected signal would miss the diffraction grating. The second lens in the system was used to collect the diverging beam and focus it onto the detector. Because the signals arriving at the detector were so small, the preamplifier and the lock-in amplifier were set with large gains. As a consequence, the system was very sensitive to noise. This setup was never used to test actual crystals because a commercial monochromator was procured for this project, and a new station was built using some of the components from this system.

Single Sweep Monochromator. A commercial monochromator (Acton Research Corp. SpectraPro-150) was the foundation for a more simplified setup.

The monochromator had a few features that made it more suitable for taking reflectance measurements. The monochromator was motorized and could be controlled with either a remote scan controller or a PC. Unlike the first reflectance setup, the wavelength of light exiting the device could be directly specified by typing it into the scan controller. The slits were variable (0- 3mm) so that the resolution could be easily changed. This commercial monochromator had a specified resolution of 0.4nm with 10 μ m wide by 4mm high slits and a standard 1200groove/mm grating. The two gratings supplied with the monochromator were a 300groove/mm grating with a 2 μ m blaze angle and a 150groove/mm grating with a 4 μ m blaze angle. These two gratings can cover the necessary 2-6 μ m scan range.

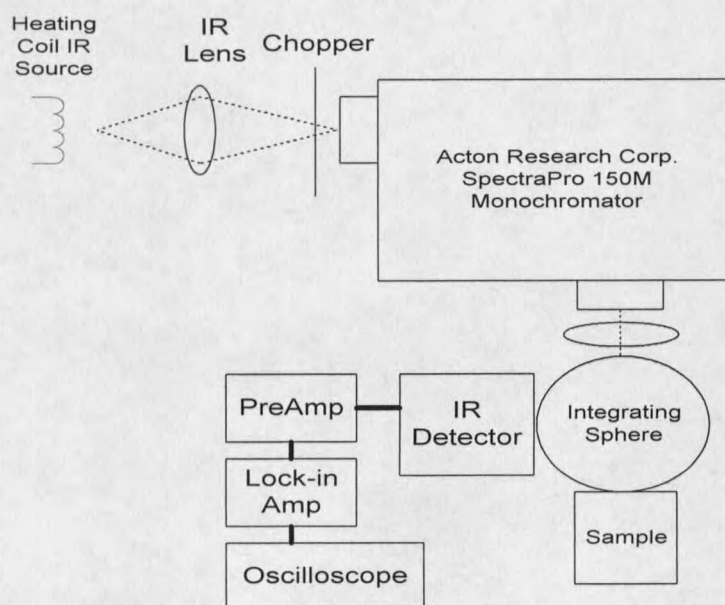


Figure 4-11: Reflectance layout using the monochromator.

The original setup for the monochromator is shown in Figure 4-11. The setup used a gold integrating sphere to collect reflections from the crystal sample. The integrating sphere was used to eliminate any angle dependence inherent in the reflections. The inside of the integrating sphere is a rough surface coated with gold, which is one hundred percent reflective in the IR. Light that gets trapped in the sphere is diffused. This causes light at the exit port to simulate a perfect Lambertian source. Unfortunately after the station was assembled and tested, the signal leaving the monochromator was not strong enough to be used with the integrating sphere. There is usually a loss of signal when light is diffused. This is due in part to the diffusion process where the light is reflected in random directions. The integrating sphere was removed from the system, and a new layout was designed. The new layout is shown in Figure 4-12.

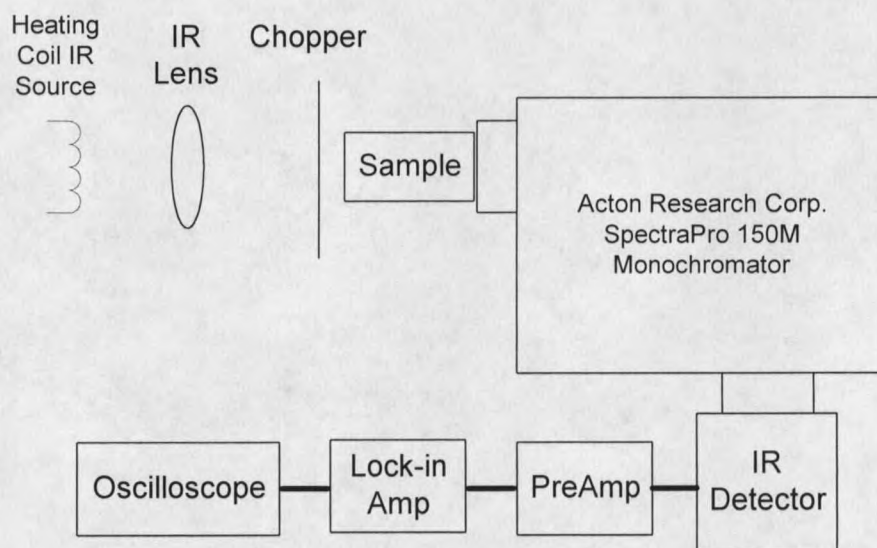


Figure 4-12: Revised monochromator setup.

This layout measured transmittance, not reflectance. When measuring reflectance peaks by looking at transmittance, the signal will look like a notch instead of a peak. This was not the most desirable setup, but it was suitable for this project. The doped YAG has absorption peaks that can look like notches due to a Bragg reflection. Looking at the transmittance of a doped YAG crystal with no striae minimized this effect.

This setup was checked and calibrated by again using the band pass filters. The filters were placed at the sample position and data was taken. The data sheets for the filters and the corresponding scans using this setup are in Appendix C.

A major problem was encountered using this setup. Since the monochromator uses a diffraction grating to achieve wavelength selectability, higher orders from shorter wavelengths will also pass through the system. This means that 2275nm light will propagate through the system even when it is set for 4550nm. This effect was first noticed when the light greater than $6\mu\text{m}$ was propagating through the YAG crystals. Using high pass filters with cut on wavelengths of $2\mu\text{m}$ and $4\mu\text{m}$ solved this problem.

Crystal 1-525B was the first to be tested. Four scans were made with the monochromator to cover the region from $2\mu\text{m}$ to $6\mu\text{m}$. The $2\mu\text{m}$ long pass filter was used to scan between $2\mu\text{m}$ and $4\mu\text{m}$. Scanning any further would again introduce the higher orders of light from the shorter wavelengths. A scan was also made without the crystal to reference the background light. The filters and monochromator all have some wavelength dependence that affects the transmission

measurements. This effect can be accounted for by dividing the transmission waveform of the crystal by the reference waveform. This creates a normalized signal where fluctuations are due to only the crystal. This method yielded an average signal to noise ratio of 22:1. Fluctuations of more than five percent should be measurable with this setup. Two more scans were made using the 4 μm long pass filter to take measurements between 4 μm and 6 μm . With the crystal in the system the signal drops to zero past 6 μm . There were no apparent reflection notches between 4 μm and 6 μm .

The next crystals tested were 2-561 Top, Middle, and Bottom because the measured pitches were small enough to create a Bragg grating reflection within the transmission band of YAG. Figure 4-13 shows an example of the transmission measurements.

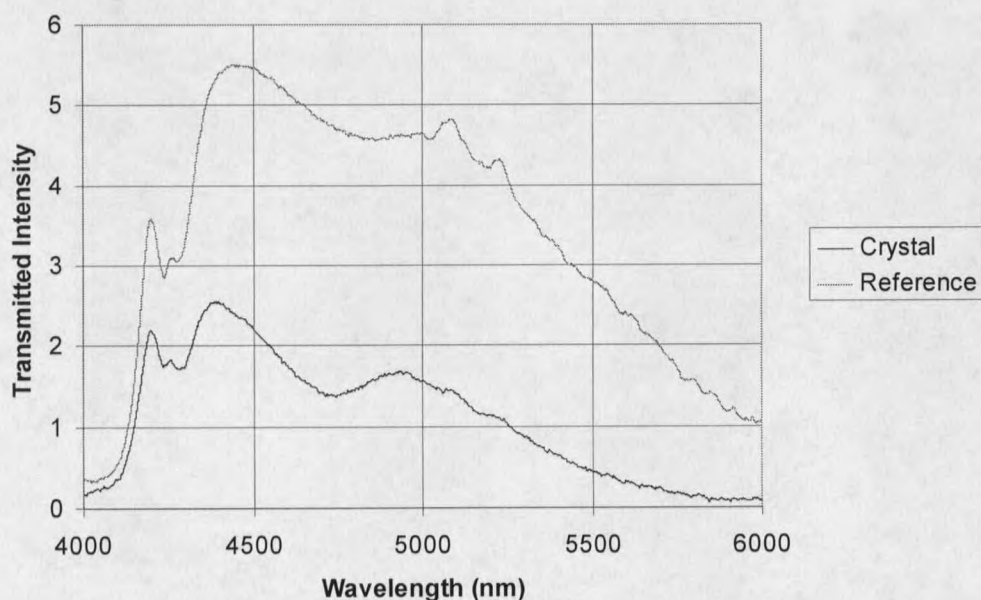


Figure 4-13: Transmission of 4 μm to 6 μm light through crystal 2-561.

